Contents lists available at ScienceDirect

Computer Physics Communications

journal homepage: www.elsevier.com/locate/cpc



Efficient and linear schemes for anisotropic Cahn-Hilliard model using the Stabilized-Invariant Energy Quadratization (S-IEQ) approach



Zhen Xu^a, Xiaofeng Yang ^{b,*}, Hui Zhang ^{a,c}, Ziqing Xie ^d

- ^a School of Mathematics Sciences, Beijing Normal University, Beijing, 100875, PR China
- ^b Department of Mathematics, University of South Carolina, Columbia, SC, 29208, USA
- ^c Laboratory of Mathematics and Complex Systems, Ministry of Education, PR China
- d LCSM(MOE) and School of Mathematics and Statistics, Hunan Normal University, Changsha, Hunan, 410081, PR China

ARTICLE INFO

Article history: Received 25 June 2018 Received in revised form 9 November 2018 Accepted 21 December 2018 Available online 7 January 2019

Keywords: Anisotropy Phase-field Cahn-Hilliard Energy stability IEQ method Second-order

ABSTRACT

In this paper, we consider numerical approximations for the anisotropic Cahn–Hilliard equation. We develop two linear and second-order schemes that combine the IEQ approach with the stabilization technique, where several extra linear stabilization terms are added in and they can be shown to be crucial to suppress the non-physical spatial oscillations caused by the strong anisotropy. We show the well-posedness of the resulting linear systems and further prove their corresponding unconditional energy stabilities rigorously. Various 2D and 3D numerical simulations are presented to demonstrate the stability, accuracy, and efficiency of the proposed schemes.

© 2018 Elsevier B.V. All rights reserved.

1. Introduction

In this paper, we consider numerical approximations for solving the anisotropic Cahn-Hilliard equation, which was proposed in [1,2] to simulate the formation of faceted pyramids on nanoscale crystal surfaces. Its counterpart, the isotropic Cahn-Hilliard equation, is a typical system of the diffusive phase field model and has been widely used in modeling/simulations for the free interface problems, see [3–6] and the references therein. About time marching schemes for solving the isotropic Cahn-Hilliard equation, there exists quite a few prevalent numerical methods, for instances, the fully-explicit [7], fully-implicit [8], convex-splitting [9–14], linear stabilization [7,15,16], Invariant Energy Quadratization (IEQ) method [14,17-25], and its variant version Scalar Auxiliary Variable (SAV) method [26], etc. All these methods aim to construct schemes that can either verify the property at the discrete level irrespectively of the coarseness of the temporal discretization (called energy stable or thermodynamically consistent) or identify the stability condition on the time step. Since the coarse-graining (macroscopic) process may undergo rapid changes near the interface, the noncompliance of energy dissipation laws may lead to spurious numerical solutions if the grid and time step sizes are not carefully controlled.

Comparing to the isotropic Cahn-Hilliard model, in addition to the stiffness issue from the thin interfacial width, the numerical challenge of constructing energy stable schemes for the anisotropic system focuses on how to design the proper discretization for the nonlinear terms multiplied with the strong anisotropic coefficient. These terms increase the complexity for algorithm developments to a large extent since they can induce large non-physical spatial oscillations. Therefore, it is remarkable that there are very few successful attempts at designing efficient and energy stable time marching schemes for this model. In [27], the authors discretized the anisotropic nonlinear term in the explicit way, that resulted in severe time step restrictions. In [1,2], the authors developed a second-order fully-implicit scheme based on the Crank-Nicolson type approach. Its energy stability/solvability are not only questionable theoretically, but the implementation is also complicated due to the nonlinear nature. In [28], the authors developed an unconditionally stable scheme that can work for a class of convex type anisotropy. However, their method is not applicable since the anisotropy we consider in this paper is non-convex instead. In [29], the authors developed a first-order time marching scheme based on the linear stabilization method. Although the method is very easy to implement and quite robust in computations, there are still no clues on how to prove its energy stability theoretically thus far. In [30], the authors applied the convex splitting approach for solving this model, however, the energy stability is not provable for anisotropic case. In [31], the authors proposed a second-order

^{*} Corresponding author.

E-mail addresses: xuzhenmath@mail.bnu.edu.cn (Z. Xu), xfyang@math.sc.edu
(X. Yang), hzhang@bnu.edu.cn (H. Zhang), ziqingxie@hunnu.edu.cn (Z. Xie).

scheme that is actually the modified version of the linear stabilization scheme in [29], where the second order extrapolation is preestimated by the solutions of the first-order scheme. However, it is not clear on how to prove such a scheme to be energy stable.

Therefore, in this paper, we aim to develop efficient and provably energy stable time marching schemes for the anisotropic Cahn-Hilliard model. We use the recently developed IEQ approach since it can always produce easy-to-implement (linear) and unconditionally energy stable schemes. However, this anisotropic model is so special that the spatial oscillations can induce severe instability on the time step. In other words, the formally energy stable IEQ method is found to reach such a bottleneck: it still blows up even when using very small time steps (shown in Fig. 4.7). To fix such an inherent deficiency, we combine the IEO approach with the stabilization technique which we arrive at a novel stabilized-IEQ (S-IEQ) method. More precisely, by adding several linear stabilizing terms and treating all involved nonlinear terms in the semiexplicit way, a unconditionally energy stable scheme is obtained, theoretically and numerically. These stabilizing terms can not only enhance energy stability while keeping the required accuracy, but also are the keys to prove the well-posedness of the linear system.

Overall, the proposed S-IEQ schemes possess the following three desired properties, i.e., (i) accurate (second order in time); (ii) energy stable (unconditional energy law holds); and (iii) easyto-implement. To the best of the authors' knowledge, the proposed S-IEQ scheme is the first scheme for the anisotropic Cahn-Hilliard system that can be theoretically proved to be energy stable. Through the comparisons with two other prevalent numerical schemes such as the linear-stabilized scheme [29] and the IEO scheme (without stabilizers) for a number of classical benchmark numerical examples, we demonstrate the stability and the accuracy of the proposed S-IEQ schemes as well.

The rest of the paper is organized as follows. In Section 2, we give a brief introduction to the governing PDE system. In Section 3, we present second-order schemes for the anisotropic model with linear and the Willmore regularizations, respectively. The unconditional energy stability and the well-posedness of the linear systems are proved rigorously. In Section 4, we implement various 2D and 3D numerical simulations to demonstrate the stability and accuracy of the proposed numerical schemes. Some concluding remarks are given in Section 5.

2. Anisotropic Cahn-Hilliard equations

Now we give a brief description for the anisotropic Cahn-Hilliard equation, that describes binary mixture with the anisotropic interfacial energy [1,2]. Let Ω be a smooth, open, bounded, connected domain in \mathbb{R}^d with d=2,3, and ϕ be an order parameter which takes the values ± 1 in the two phases with a smooth transitional layer of thickness ϵ . The total free energy of the system is given in the following form,

$$E(\phi) = \int_{\Omega} \left(\gamma(\mathbf{n}) \left(\frac{1}{2} |\nabla \phi|^2 + \frac{1}{\epsilon^2} F(\phi) \right) + \frac{\beta}{2} G(\phi) \right) d\mathbf{x}, \tag{2.1}$$

where $\gamma(\mathbf{n})$ is a function describing the anisotropic property and \mathbf{n} is the interfacial normal defined as

$$\mathbf{n} = \frac{\nabla \phi}{|\nabla \phi|},\tag{2.2}$$

and the fourfold symmetric anisotropic function is given by

$$\gamma(\mathbf{n}) = 1 + \alpha \cos(4\Theta) = 1 + \alpha(4\sum_{i=1}^{d} n_i^4 - 3), \tag{2.3}$$

where Θ denotes the orientation angle of the interfacial normal to the interface. The non-negative parameter α in (2.3) describes the intensity of anisotropy. When $\alpha = 0$, the system degenerates to the isotropic model, and when α increases, the anisotropy becomes stronger. The energy density $F(\phi)$ takes the usual double-well form $F(\phi) = \frac{1}{4}(\phi^2 - 1)^2$. The potential $G(\phi)$ is added to penalize infinite curvatures in the resulting corners and β is the magnitude of the regularization parameter. Two kinds of regularization terms are usually considered. The first one is the linear regularization that

$$G_l(\phi) = (\Delta \phi)^2; \tag{2.4}$$

and the second one, which is more effective as an approximation to the consistent sharp-interface model as pointed out in [1], is the nonlinear Willmore regularization that reads as,

$$G_W(\phi) = \left(\Delta\phi - \frac{1}{\epsilon^2} f(\phi)\right)^2,\tag{2.5}$$

where $f(\phi) = F'(\phi) = \phi(\phi^2 - 1)$. By taking the H^{-1} gradient flow of the total free energy (2.1), we arrive at the anisotropic Cahn-Hilliard system with the linear regularization that reads as:

$$\phi_t = \nabla \cdot (M(\phi)\nabla \mu), \tag{2.6}$$

$$\mu = -\nabla \cdot \mathbf{m} + \frac{\gamma(\mathbf{n})}{\epsilon^2} f(\phi) + \beta \Delta^2 \phi, \tag{2.7}$$

where $M(\phi)$ is the mobility function with $M(\phi) \ge M_0 > 0$; or with the Willmore regularization that reads as:

$$\phi_t = \nabla \cdot (M(\phi)\nabla \mu), \tag{2.8}$$

$$\mu = -\nabla \cdot \mathbf{m} + \frac{\gamma(\mathbf{n})}{\epsilon^2} f(\phi) + \beta \left(\Delta - \frac{1}{\epsilon^2} f'(\phi) \right)$$

$$\times \left(\Delta \phi - \frac{1}{\epsilon^2} f(\phi)\right),\tag{2.9}$$

where the vector field **m** is defined as

$$\mathbf{m} = \gamma(\mathbf{n})\nabla\phi + \frac{\mathbb{P}\nabla_{\mathbf{n}}\gamma(\mathbf{n})}{|\nabla\phi|} \left(\frac{1}{\epsilon^2}F(\phi) + \frac{1}{2}|\nabla\phi|^2\right),\tag{2.10}$$

with $\mathbb{P} = \mathbb{I} - \boldsymbol{n}\boldsymbol{n}^T$.

Note that the expression for **m** may cause significant difficulties in numerical simulation due to the term $\frac{1}{|\nabla \phi|} \frac{F(\phi)}{\epsilon^2}$. We use the asymptotic result that the following fact holds near the interface

$$F(\phi) \sim \frac{\epsilon^2}{2} |\nabla \phi|^2.$$
 (2.11)

Thus the vector **m** can be rewritten as

$$\mathbf{m} = \gamma(\mathbf{n})\nabla\phi + \mathbb{P}\nabla_{\mathbf{n}}\gamma(\mathbf{n})|\nabla\phi|. \tag{2.12}$$

For simplicity, we adopt the periodic boundary conditions to remove all complexities associated with the boundary integrals in this study. We remark that the boundary conditions can also be the no-flux type as

$$\frac{\partial \phi}{\partial \mathbf{n}}\Big|_{\partial \Omega} = \frac{\partial \mu}{\partial \mathbf{n}}\Big|_{\partial \Omega} = \frac{\partial \omega}{\partial \mathbf{n}}\Big|_{\partial \Omega} = 0, \tag{2.13}$$

where $w = \Delta \phi$ for linear regularization model and $w = \Delta \phi$ – $\frac{1}{2}f(\phi)$ for the Willmore regularization model, **n** is the outward normal of the computational domain Ω . All numerical analysis in this paper can be carried out to the no-flux boundary conditions without any further difficulties. Note we also define $\bf n$ as the interfacial normal in the model and anisotropic equations, which might not be confused by the readers.

The model equations (2.6)–(2.7) and (2.8)-(2.9) follow the dissipative energy law. By taking the L^2 inner product of (2.6) with $-\mu$, and of (2.7) with ϕ_t , using the integration by parts and combining the obtained two equalities, we obtain

$$\frac{d}{dt}E(\phi) = -\|\sqrt{M(\phi)}\nabla\mu\|^2 \le 0. \tag{2.14}$$

In addition, the Cahn–Hilliard type dynamical system (2.6)–(2.7) and (2.8)–(2.9) conserve the local mass density. By taking the L^2 inner product of (2.6) with 1, one can obtain the mass conservation property directly using integration by parts, that reads as

$$\frac{d}{dt} \int_{\Omega} \phi(\mathbf{x}, t) d\mathbf{x} = 0. \tag{2.15}$$

3. Numerical schemes

We fix some notations here. We denote $\delta t>0$ the time step size and set $t^n=n\delta t$ for $0\leq n\leq N$ with $T=N\delta t$. Then we denote the L^2 inner product of any two spatial functions $f_1(\textbf{x})$ and $f_2(\textbf{x})$ by $(f_1(\textbf{x}),f_2(\textbf{x}))=\int_{\Omega}f_1(\textbf{x})f_2(\textbf{x})d\textbf{x}$, and the L^2 norm of the function f(x) by $\|f\|=(f,f)^{\frac{1}{2}}$. We also define the following Sobolev spaces $H^k_{per}(\Omega)=\{\phi \text{ is periodic}, \int_{\Omega}\phi d\textbf{x}=0, \phi\in H^k(\Omega)\}$ with k=1,2.

3.1. Linear regularization model

We first deal with the linear regularization model. By using the IEQ approach, an auxiliary variable U is defined as

$$U = \sqrt{\gamma(\mathbf{n})\left(\frac{1}{2}|\nabla\phi|^2 + \frac{1}{\epsilon^2}F(\phi)\right) + B},\tag{3.1}$$

where $B(\sim O(\frac{1}{\epsilon^2}))$ is a constant that ensures the radicand positive. Therefore the total free energy (2.1) can be expressed as

$$E(\phi, U) = \int_{\Omega} \left(U^2 - B + \frac{\beta}{2} (\Delta \phi)^2 \right) d\mathbf{x}. \tag{3.2}$$

Using the new variable U, we then obtain an equivalent system as

$$\phi_t = \nabla \cdot (M(\phi)\nabla \mu), \tag{3.3}$$

$$\mu = HU + \beta \Delta^2 \phi, \tag{3.4}$$

$$U_t = \frac{1}{2}H\phi_t,\tag{3.5}$$

where

$$H(\phi) = \frac{-\nabla \cdot \mathbf{m} + \frac{1}{\epsilon^2} \gamma(\mathbf{n}) f(\phi)}{\sqrt{\gamma(\mathbf{n}) \left(\frac{1}{2} |\nabla \phi|^2 + \frac{1}{\epsilon^2} F(\phi)\right) + B}}.$$
(3.6)

The initial conditions for ϕ and U read as

$$\phi(t=0) = \phi^{0},$$

$$U(t=0) = \sqrt{\gamma(\mathbf{n}^{0})(\frac{1}{2}|\nabla\phi^{0}|^{2} + \frac{1}{\epsilon^{2}}F(\phi^{0})) + B},$$
(3.7)

and the boundary conditions of the new system are still same as the original system (2.6)–(2.7).

The transformed system (3.3)–(3.5) also follows an energy dissipative law in terms of ϕ and the new variable U. By taking the L^2 inner product of (3.3) with μ , of (3.4) with ϕ_t , of (3.5) with 2U, performing integration by parts and summing all equalities up, we can obtain the energy dissipation law of the new system (3.3)–(3.5) that reads as

$$\frac{d}{dt}E(\phi, U) = -\|\sqrt{M(\phi)}\nabla\mu\|^2 \le 0.$$
(3.8)

Now we present the second-order Adam–Bashforth time stepping scheme as follows.

Scheme 3.1. Having computed $(\phi, U)^n$ and $(\phi, U)^{n-1}$, we update $(\phi, U)^{n+1}$ by solving

$$\frac{3\phi^{n+1} - 4\phi^n + \phi^{n-1}}{2\delta t} = \nabla \cdot \left(M(\phi^{\star, n+1}) \nabla \mu^{n+1} \right), \tag{3.9}$$

$$\mu^{n+1} = H^{\star,n+1}U^{n+1} + \beta \Delta^2 \phi^{n+1} + \frac{S_1}{\epsilon^2} (\phi^{n+1} - 2\phi^n + \phi^{n-1}) - S_2 \Delta(\phi^{n+1} - 2\phi^n + \phi^{n-1}),$$
(3.10)

$$3U^{n+1} - 4U^n + U^{n-1} = \frac{1}{2}H^{\star,n+1}(3\phi^{n+1} - 4\phi^n + \phi^{n-1}), \quad (3.11)$$

where $\phi^{\star,n+1} = 2\phi^n - \phi^{n-1}$, and $H^{\star,n+1} = H(2\phi^n - \phi^{n-1})$. The boundary conditions are

(i) all variables are periodic; or (ii)
$$\partial_{\mathbf{n}}\phi^{n+1}|_{\partial\Omega} = \nabla\mu^{n+1} \cdot \mathbf{n}|_{\partial\Omega} = 0.$$
 (3.12)

Remark 3.1. Scheme (3.9)–(3.11) is totally linear where the nonlinear terms are treated by compositions of implicit and explicit discretization at t^{n+1} . To enhance the stability, we add two secondorder linear stabilizers (associated with S_1 and S_2) in (3.10). When both of them vanish, the scheme becomes the IEQ type scheme that had been developed in literatures, see [14,17-19,21-24,32–34]. The first term, $\frac{S_1}{\epsilon^2}(\phi^{n+1} - 2\phi^n + \phi^{n-1})$, is actually a well-known stabilizer used in the linear stabilization approach to balance the explicit treatment of the $\frac{1}{\epsilon^2}f(\phi)$ for solving the isotropic phase field model (cf. [7]). Similarly, the second stabilizer, $-S_2\Delta(\phi^{n+1}-2\phi^n+\phi^{n-1})$, is used to balance the explicit treatment of the gradient term with the anisotropic coefficient. The errors that these two terms introduced are of order $\frac{S_1}{c^2}\delta t^2\phi_{tt}(\cdot)$ and $S_2 \delta t^2 \Delta \phi_{tt}(\cdot)$, respectively, which are of the same order as the errors induced by the second order extrapolation for the nonlinear term $f(\phi)$ and the gradient term with the anisotropic coefficient. Numerical examples show that these two stabilizers are crucial to removing all oscillations induced by the anisotropic coefficient $\gamma(\boldsymbol{n})$, since the term $\boldsymbol{n} = \frac{\nabla \phi}{|\nabla \phi|}$ changes its sign frequently in the bulk part where $|\nabla \phi|$ is close to zero (cf. Fig. 4.4).

Note that the new variable U will not bring up extra computational cost due to the following procedure. We first rewrite (3.11) as follows,

$$U^{n+1} = \frac{1}{2} H^{\star, n+1} \phi^{n+1} + A^n, \tag{3.13}$$

where $A^n=\frac{4U^n-U^{n-1}}{3}-\frac{1}{2}H^{\star,n+1}\frac{4\phi^n-\phi^{n-1}}{3}$, and substitute (3.13) into (3.10), then we obtain the following linear system as follows

$$\phi^{n+1} - \frac{2\delta t}{3} \nabla \cdot \left(M(\phi^{\star,n+1}) \nabla \mu^{n+1} \right) = f_1^n, \tag{3.14}$$

$$-\mu^{n+1} + P(\phi^{n+1}) = f_2^n, \tag{3.15}$$

where

$$\begin{cases} P(\phi) = \frac{1}{2} H^{\star,n+1} H^{\star,n+1} \phi + \beta \Delta^2 \phi + \frac{S_1}{\epsilon^2} \phi - S_2 \Delta \phi, \\ f_1^n = \frac{4\phi^n - \phi^{n-1}}{3}, \\ f_2^n = -H^{\star,n+1} A^n + \frac{S_1}{\epsilon^2} \phi^{\star,n+1} - S_2 \Delta \phi^{\star,n+1}. \end{cases}$$
(3.16)

Therefore, we can solve ϕ^{n+1} and μ^{n+1} directly from (3.14)–(3.15) and then update U^{n+1} from (3.13).

Furthermore, the linear operator $P(\phi)$ is symmetric positive definite. More precisely, for any ϕ , μ with the boundary condition (3.12), we have

$$(P(\phi), \psi) = \frac{1}{2} (H^{\star, n+1} \phi, H^{\star, n+1} \psi) + \frac{S_1}{\epsilon^2} (\phi, \psi) + S_2(\nabla \phi, \nabla \psi) + \beta(\Delta \phi, \Delta \psi) = (P(\psi), \phi),$$

that means $P(\phi)$ is symmetric (self-adjoint). For any ϕ with mean zero, we have

$$(P(\phi),\phi) = \frac{1}{2} \|H^{\star,n+1}\phi\|^2 + \frac{S_1}{\epsilon^2} \|\phi\|^2 + S_2 \|\nabla\phi\|^2 + \beta \|\Delta\phi\|^2 \ge 0,$$

where "=" is valid if and only if $\phi = 0$.

We now show the well-posedness of the associated weak form for the linear system (3.14)–(3.15). In the following arguments, we will only consider the periodic boundary condition for convenience. All derivations can be easily applied to the no-flux conditions without any essential difficulties.

Define $\bar{\phi}=\frac{1}{|\Omega|}\int_{\Omega}\phi d\mathbf{x}$, and $\bar{\mu}=\frac{1}{|\Omega|}\int_{\Omega}\mu d\mathbf{x}$. By taking the L^2 inner product of (3.14) with 1, we can deduce that $\bar{\phi}^{n+1}=\bar{\phi}^n=\cdots=\bar{\phi}^0$, where $\bar{\phi}^1=\bar{\phi}^0$ comes from the corresponding first-order scheme.

Let $\phi=\phi^{n+1}-\bar{\phi}^0$ and $\mu=\mu^{n+1}-\bar{\mu}^{n+1}$, such that $\phi\in H^2_{per}(\Omega), \mu\in H^1_{per}(\Omega)$. The weak form of (3.14)–(3.15) can be written as the following system with the unknowns $(\mu,\phi)\in (H^1_{per},H^2_{per})(\Omega)$,

$$\begin{split} (\phi, w) + \frac{2\delta t}{3} \Big(M(\phi^{\star, n+1}) \nabla \mu, \nabla w \Big) &= (f_1^n - \bar{\phi}^0, w), \\ -(\mu, \psi) + \frac{1}{2} (H^{\star, n+1} \phi, H^{\star, n+1} \psi) + \frac{S_1}{\epsilon^2} (\phi, \psi) \\ + S_2(\nabla \phi, \nabla \psi) + \beta (\Delta \phi, \Delta \psi) &= (f_2^n + \bar{\mu}^{n+1} + P(\bar{\phi}_0), \psi), \end{split}$$
(3.18)

for any $(w, \psi) \in (H^1_{per}, H^2_{per})(\Omega)$.

We denote the above bilinear system (3.17)–(3.18) as

$$(\mathbf{A}(\mathbf{X}), \mathbf{Y}) = (\mathbf{B}, \mathbf{Y}), \tag{3.19}$$

where $\boldsymbol{X}=(\mu,\phi)^T$ and $\boldsymbol{Y}=(w,\psi)^T$, and both of them are in $(H^1_{per},H^2_{per})(\Omega)$.

The well-posedness of the weak system (3.17)–(3.18) is shown as follows.

Theorem 3.1. The linear system (3.17)–(3.18) admits a unique solution $(\mu, \phi)^T \in (H^1_{ner}, H^2_{ner})(\Omega)$.

Proof. (i) For any $\mathbf{X} = (\mu, \phi)^T$ and $\mathbf{Y} = (w, \psi)^T$, with $\mathbf{X}, \mathbf{Y} \in (H^1_{ner}, H^2_{ner})(\Omega)$, we derive

$$(\mathbf{A}(\mathbf{X}), \mathbf{Y}) \le C_1(\|\phi\|_{H^2} + \|\mu\|_{H^1})(\|\psi\|_{H^2} + \|w\|_{H^1}), \tag{3.20}$$

where C_1 depends on δt , ϵ , β , S_1 , S_2 , $\|M(\phi^{\star,n+1})\|_{L^{\infty}}$, and $\|H^{\star,n+1}\|_{L^{\infty}}$. Therefore, the bilinear form (A(X), Y) is bounded.

(ii) For any $\mathbf{X} = (\mu, \phi)^T \in (H^1_{per}, H^2_{per})(\Omega)$, we derive

$$(\mathbf{A}(\mathbf{X}), \mathbf{X}) = \frac{2\delta t}{3} \|\sqrt{M(\phi^{\star, n+1})} \nabla \mu\|^2 + \frac{1}{2} \|H^{\star, n+1} \phi\|^2 + \frac{S_1}{\epsilon^2} \|\phi\|^2 + S_2 \|\nabla \phi\|^2 + \beta \|\Delta \phi\|^2 \geq C_2 (\|\mu\|_{H^1}^2 + \|\phi\|_{H^2}^2),$$
(3.21)

where C_2 depends on δt , ϵ , β , S_1 , S_2 , and M_0 . Thus the bilinear form (A(X), Y) is coercive. Then from the Lax–Milgram theorem, we conclude the linear system (3.14)–(3.15) admits a unique solution $(\mu, \phi)^T \in (H^1_{per}, H^2_{per})(\Omega)$. \square

The energy stability of the scheme (3.9)–(3.11) is shown as follows.

Theorem 3.2. The scheme (3.9)–(3.11) is unconditionally energy stable which satisfies the following discrete energy dissipation law,

$$\frac{1}{\delta t} (E_L^{n+1} - E_L^n) \le -\|\sqrt{M(\phi^{\star, n+1})} \nabla \mu^{n+1}\|^2 \le 0, \tag{3.22}$$

where

$$E_L^{n+1} = \left(\frac{\|U^{n+1}\|^2}{2} + \frac{\|2U^{n+1} - U^n\|^2}{2}\right) + \frac{\beta}{2} \left(\frac{\|\Delta\phi^{n+1}\|^2}{2} + \frac{\|2\Delta\phi^{n+1} - \Delta\phi^n\|^2}{2}\right), + \frac{S_1}{\epsilon^2} \frac{\|\phi^{n+1} - \phi^n\|^2}{2} + S_2 \frac{\|\nabla\phi^{n+1} - \nabla\phi^n\|^2}{2} - B|\Omega|.$$
(3.23)

Proof. By taking the L^2 inner product of (3.9) with $-2\delta t \mu^{n+1}$, we obtain

$$-(3\phi^{n+1} - 4\phi^n + \phi^{n-1}, \mu^{n+1})$$

$$= 2\delta t \|\sqrt{M(\phi^{\star,n+1})}\nabla \mu^{n+1}\|^2.$$
(3.24)

By taking the L^2 inner product of (3.10) with $3\phi^{n+1} - 4\phi^n + \phi^{n-1}$, we obtain

$$\begin{split} &(\mu^{n+1}, 3\phi^{n+1} - 4\phi^n + \phi^{n-1}) \\ &= \left(H^{\star, n+1}U^{n+1}, 3\phi^{n+1} - 4\phi^n + \phi^{n-1}\right) \\ &+ \beta(\Delta\phi^{n+1}, 3\Delta\phi^{n+1} - 4\Delta\phi^n + \Delta\phi^{n-1}) \\ &+ \frac{S_1}{\epsilon^2}(\phi^{n+1} - 2\phi^{n+1} + \phi^{n-1}, 3\phi^{n+1} - 4\phi^n + \phi^{n-1}) \\ &+ S_2(\nabla\phi^{n+1} - 2\nabla\phi^{n+1} + \nabla\phi^{n-1}, 3\nabla\phi^{n+1} - 4\nabla\phi^n + \nabla\phi^{n-1}) \end{split}$$

By taking the L^2 inner product of (3.11) with $-2U^{n+1}$, we obtain

$$-2(3U^{n+1} - 4U^n + U^{n-1}, U^{n+1})$$

$$= -(H^{\star, n+1}(3\phi^{n+1} - 4\phi^n + \phi^{n-1}), U^{n+1}).$$
(3.25)

By combining these above equations and applying the following identities,

$$2a(3a - 4b + c) = a^{2} - b^{2} + (2a - b)^{2}$$
$$- (2b - c)^{2} + (a - 2b + c)^{2},$$
$$(a - 2b + c)(3a - 4b + c) = (a - b)^{2} - (b - c)^{2}$$
$$+ 2(a - 2b + c)^{2},$$

we obtain

$$\begin{split} & (\frac{1}{2}\|U^{n+1}\|^2 + \frac{1}{2}\|2U^{n+1} - U^n\|^2 - \frac{1}{2}\|U^n\|^2 - \frac{1}{2}\|2U^n - U^{n-1}\|^2) \\ & + \frac{\beta}{2} \left(\frac{1}{2}\|\Delta\phi^{n+1}\|^2 + \frac{1}{2}\|2\Delta\phi^{n+1} - \Delta\phi^n\|^2 \right. \\ & - \frac{1}{2}\|\Delta\phi^n\|^2 - \frac{1}{2}\|2\Delta\phi^n - \Delta\phi^{n-1}\|^2) \\ & + \frac{S_1}{\epsilon^2} \left(\frac{1}{2}\|\phi^{n+1} - \phi^n\|^2 - \frac{1}{2}\|\phi^n - \phi^{n-1}\|^2\right) \\ & + S_2 \left(\frac{1}{2}\|\nabla\phi^{n+1} - \nabla\phi^n\|^2 - \frac{1}{2}\|\nabla\phi^n - \nabla\phi^{n-1}\|^2\right) \\ & + \frac{1}{2}\|U^{n+1} - 2U^n + U^{n-1}\|^2 \\ & + \frac{\beta}{4}\|\Delta\phi^{n+1} - 2\Delta\phi^n + \Delta\phi^{n-1}\|^2 \\ & + \frac{S_1}{\epsilon^2}\|\phi^{n+1} - 2\phi^n + \phi^{n-1}\|^2 \\ & + S_2\|\nabla\phi^{n+1} - 2\nabla\phi^n + \nabla\phi^{n-1}\|^2 \\ & = -\delta t\|\sqrt{M(\phi^{\star,n+1})}\nabla\mu^{n+1}\|^2. \end{split}$$

Finally, we obtain the desired result after dropping some positive terms. $\ \square$

Remark 3.2. Heuristically, $\frac{1}{\delta t}(E_L^{n+1}-E_L^n)$ is a second-order approximation of $\frac{d}{dt}E(\phi,U)$ at $t=t^{n+1}$. For any smooth variable ψ with

time, we have

$$\frac{\|\psi^{n+1}\|^{2} + \|2\psi^{n+1} - \psi^{n}\|^{2}}{2\delta t} - \frac{\|\psi^{n}\|^{2} + \|2\psi^{n} - \psi^{n-1}\|^{2}}{2\delta t}$$

$$\cong \frac{\|\psi^{n+2}\|^{2} - \|\psi^{n}\|^{2}}{2\delta t} + O(\delta t^{2})$$

$$\cong \frac{d}{dt} \|\psi(t^{n+1})\|^{2} + O(\delta t^{2}), \quad (3.26)$$

and

$$\frac{\|\psi^{n+1} - \psi^n\|^2 - \|\psi^n - \psi^{n-1}\|^2}{2\delta t} \cong O(\delta t^2).$$
 (3.27)

Remark 3.3. We can easily develop an alternative second-order scheme based on the Crank–Nicolson type approach, where the second-order stabilization terms are still in the same form. The corresponding well-posedness and energy stability can be proved similarly. Thus we omit the details here.

Remark 3.4. Other numerical schemes have been proposed for the anisotropic Cahn–Hilliard model under consideration. In [29], Chen and Shen proposed the first-order, stabilized-explicit schemes with linear regularization and Willmore regularization, respectively. By using the similar strategy, for the linear regularization model, we can construct a corresponding second-order stabilized-explicit scheme, it reads as

$$\frac{3\phi^{n+1} - 4\phi^{n} + \phi^{n-1}}{2\delta t} = \nabla \cdot (M(\phi^{\star,n+1})\nabla\mu^{n+1}),$$

$$\mu^{n+1} = -\nabla \cdot \mathbf{m}^{\star,n+1} + \frac{\gamma(\mathbf{n}^{\star,n+1})}{\epsilon^{2}} f(\phi^{\star,n+1})$$

$$+ \beta \Delta^{2}\phi^{n+1}$$

$$+ \frac{S_{1}}{\epsilon^{2}} (\phi^{n+1} - 2\phi^{n} + \phi^{n-1}) - S_{2}\Delta$$

$$\times (\phi^{n+1} - 2\phi^{n} + \phi^{n-1}),$$
(3.28)

where $\mathbf{m}^{\star,n+1} = \mathbf{m}(\phi^{\star,n+1})$. Here all nonlinear terms are treated explicitly and the exactly same two linear stabilizers are added in order to enhance the stability. In Section 4, we will compare this stabilized-explicit type scheme (with and without stabilizers) with the proposed S-IEQ schemes (3.9)–(3.11), to show the impacts of stabilizing terms on the energy stability.

3.2. Willmore regularization model

In this subsection, we construct a second-order time-stepping scheme for the anisotropic model (2.8)–(2.9) with Willmore type regularization.

Using the quadratization technique, an auxiliary variable is defined as follows.

$$V = \sqrt{\gamma(\mathbf{n})\left(\frac{1}{2}|\nabla\phi|^2 + \frac{1}{\epsilon^2}F(\phi)\right) + \frac{\beta}{2}\left(\Delta\phi - \frac{1}{\epsilon^2}f(\phi)\right)^2 + B}, \quad (3.29)$$

where B is any constant that ensures the radicand positive. Then the total free energy (2.1) can be expressed as

$$E(\phi, V) = \int_{\Omega} (V^2 - B) d\mathbf{x}. \tag{3.30}$$

Similarly, we derive an equivalent PDE system using the new variable V and ϕ , and it reads as

$$\phi_t = \nabla \cdot (M(\phi)\nabla \mu),\tag{3.31}$$

$$\mu = ZV, \tag{3.32}$$

$$V_t = \frac{1}{2} Z \phi_t, \tag{3.33}$$

where

$$Z(\phi) = \frac{-\nabla \cdot \mathbf{m} + \frac{1}{\epsilon^2} \gamma(\mathbf{n}) f(\phi) + \beta \left(\Delta - \frac{1}{\epsilon^2} f'(\phi)\right) \left(\Delta \phi - \frac{1}{\epsilon^2} f(\phi)\right)}{\sqrt{\gamma(\mathbf{n}) \left(\frac{1}{2} |\nabla \phi|^2 + \frac{1}{\epsilon^2} F(\phi)\right) + \frac{\beta}{2} \left(\Delta \phi - \frac{1}{\epsilon^2} f(\phi)\right)^2 + B}}.$$
(3.34)

The initial conditions for ϕ and V read as

$$\begin{cases} \phi(t=0) = \phi^{0}, \\ V(t=0) = \sqrt{\gamma(\mathbf{n}^{0})\left(\frac{1}{2}|\nabla\phi^{0}|^{2} + \frac{1}{\epsilon^{2}}F(\phi^{0})\right) + \frac{\beta}{2}\left(\Delta\phi^{0} - \frac{1}{\epsilon^{2}}f(\phi^{0})\right)^{2} + B}. \end{cases}$$
(3.35)

Now we present the BDF2 scheme for solving the transformed model (3.31)–(3.33) as follows.

Scheme 3.2. Assuming that $(\phi, V)^n$ and $(\phi, V)^{n-1}$ are known, we update $(\phi, V)^{n+1}$ by solving

$$\begin{split} \frac{3\phi^{n+1}-4\phi^n+\phi^{n-1}}{2\delta t} &= \nabla \cdot \left(M(\phi^{\star,n+1})\nabla \mu^{n+1}\right), \\ \mu^{n+1} &= Z^{\star,n+1}V^{n+1} \\ &+ \frac{S_1}{\epsilon^2}(\phi^{n+1}-2\phi^n+\phi^{n-1}) \\ &- S_2\Delta(\phi^{n+1}-2\phi^n+\phi^{n-1}) \\ &+ S_3\Delta^2(\phi^{n+1}-2\phi^n+\phi^{n-1}), \\ 3V^{n+1}-4V^n+V^{n-1} &= \frac{1}{2}Z^{\star,n+1}(3\phi^{n+1}-4\phi^n+\phi^{n-1}), \end{split} \tag{3.38}$$

where $\phi^{\star,n+1}=2\phi^n-\phi^{n-1}$, and $Z^{\star,n+1}=Z(2\phi^n-\phi^{n-1})$. The boundary conditions are

(i) all variables are periodic; or (ii)
$$\partial_{\mathbf{n}}\phi^{n+1}|_{\partial\Omega} = \nabla\mu^{n+1} \cdot \mathbf{n}|_{\partial\Omega} = 0.$$
(3.39)

Remark 3.5. Here we add the third second-order linear stabilizer, $S_3\Delta^2(\phi^{n+1}-2\phi^n+\phi^{n-1})$, to enhance the stability since the nonlinear term induced by the Willmore regularization potential is treated semi-explicitly. Moreover, for this model, if we set $S_1=S_2=S_3=0$, we note that it appears very difficult to show the coerciveness of the corresponding weak form, see [18]. Thus the three stabilizing terms are crucial to show the well-posedness of the resulting system. The corresponding details are not shown here since the processes are quite similar to Theorem 3.1.

The above scheme (3.36)–(3.38) is almost identical to the scheme (3.9)–(3.11) for the linear regularization model, thus we omit the details of the well-posedness, and just present the theorem of the energy stability for it as follows.

Theorem 3.3. The scheme (3.36)–(3.38) is unconditionally energy stable which satisfies the following discrete energy dissipation law,

$$\frac{1}{\delta t} (E_W^{n+1} - E_W^n) \le -\|\sqrt{M(\phi^{\star,n+1})} \nabla \mu^{n+1}\|^2 \le 0, \tag{3.40}$$

where

$$\begin{split} E_W^{n+1}(\phi,V) &= \left(\frac{\|V^{n+1}\|^2}{2} + \frac{\|2V^{n+1} - V^n\|^2}{2}\right) + \frac{S_1}{\epsilon^2} \frac{\|\phi^{n+1} - \phi^n\|^2}{2} \\ &+ S_2 \frac{\|\nabla\phi^{n+1} - \nabla\phi^n\|^2}{2} \\ &+ S_3 \frac{\|\Delta\phi^{n+1} - \Delta\phi^n\|^2}{2} - B|\Omega|. \end{split} \tag{3.41}$$

Proof. The proof is omitted since it is quite similar to Theorems 3.1 and 3.2. \Box

4. Numerical simulation

We now present various numerical simulations in 2D and 3D to demonstrate the efficiency, energy stability and accuracy of the proposed numerical schemes. The computational domain is $\Omega = [0,2\pi]^d$, d=2,3 and the Fourier-Spectral method is adopted to discretize the domain, where 128^d Fourier modes are used.

4.1. Accuracy test: mesh refinement in time

We first implement 2D simulations to test the convergence rates of these proposed S-IEQ schemes (3.9)–(3.11) and (3.36)–(3.38). In this part, $M(\phi)=\epsilon^2$ and the other order parameters are set as follows,

$$\epsilon = 6.28e - 2, B = 1e4.$$
 (4.1)

To see how the stability/accuracy is affected by the linear stabilizing terms, we will compare the numerical results computed by four schemes, i.e., the stabilized-explicit scheme (3.28) (denoted by S-LS) and its counterpart: the linear explicit scheme (3.28) with $S_1 = S_2 = 0$ (denoted by LS); the stabilized IEQ scheme (3.9)–(3.11) (denoted by S-IEQ) and its counterpart: the IEQ scheme (3.9)–(3.11) with $S_1 = S_2 = 0$ (denoted by IEQ).

We set the initial condition as follows,

$$\phi_0(x, y) = \tanh\left(\frac{\sqrt{(x-\pi)^2 + (y-\pi)^2} - 1.7}{2\epsilon}\right). \tag{4.2}$$

Since the exact solutions are not known, we choose the solution obtained with the time step size $\delta t = 1e-8$ as the benchmark solution (approximately the exact solution) for computing errors.

We set the anisotropy parameter $\alpha=0.1$ and regularization parameter $\beta=6\mathrm{e}{-4}$ for both models. The accuracy test for the linear regularization model is shown in Fig. 4.1(a), where we compare the numerical L^2 errors of the phase variable between the numerical solution and the benchmark solution at $t=1\mathrm{e}{-3}$ with different time step sizes. For S-LS and S-IEQ schemes, the stabilizing constants are $S_1=S_2=4$. Some remarkable features observed from Fig. 4.1(a) are listed as follows.

- We observe that the S-IEQ and S-LS schemes can achieve almost perfect second-order accuracy in time.
- When $\delta t > 6.25 \mathrm{e} 6$, the LS scheme blows up therefore the accuracy points are missing, and the IEQ scheme presents no order of accuracy. When $\delta t < 6.25 \mathrm{e} 6$, the LS scheme presents the second-order accuracy and the order of the IEQ scheme is a little bit worse than that of the LS scheme.
- When $\delta t < 6.25 e-6$, all four schemes achieve almost perfect second-order accuracy in time. But obviously, the magnitude of errors computed by the S-LS and S-IEQ schemes are bigger than that computed by the LS and IEQ schemes. This phenomenon is reasonable since the added stabilizers actually increase the splitting errors indeed.

For the case of Willmore regularization model, we compare the performance of the IEQ and S-IEQ methods. We set $S_1=S_2=4$, $S_3=2.4\mathrm{e}{-3}$ in the S-IEQ scheme. In Fig. 4.1(b), we compare the numerical L^2 errors of the phase variable ϕ between the numerical solution and the benchmark solution at $t=1\mathrm{e}{-3}$ with different time step sizes. We observe that the S-IEQ scheme can achieve almost perfect second-order accuracy in time. But for IEQ scheme, when $\delta t > 7.8125\mathrm{e}{-7}$, it blows up thus most accuracy points are missing, and presents no accuracy.

Therefore, from these two accurate tests, when concerning the stability, we find that the two stabilized schemes (S-LS and S-IEQ) can conquer their non-stabilized versions (LS and IEQ). Meanwhile, these two stabilized schemes are comparable and one cannot tell

any obvious differences between them, from any point of view of the stability and/or accuracy.

4.2. Isotropic case with linear regularization

In this example, we consider the isotropic model ($\alpha=0$) with the linear regularization where we still set $\beta=6\mathrm{e}{-4}$. In the following simulation, $M(\phi)=1$ and all other parameters are from (4.1). We adopt the S-IEQ scheme with $S_1=S_2=4$. The initial condition reads as follows,

$$\phi_0(x, y) = \sum_{i=1}^{2} \tanh\left(\frac{\sqrt{(x - x_i)^2 + (y - y_i)^2} - r_i}{1.2\epsilon}\right) - 1,$$
(4.3)

where $(x_1, y_1, r_1) = (1.1\pi, 0.9\pi, 0.45\pi)$ and $(x_2, y_2, r_2) = (0.5\pi, 1.5\pi, 0.15\pi)$.

We note that any time step size δt is allowable for the computations from the stability concern since the developed S-IEQ scheme is unconditionally energy stable. But larger time step can induce larger numerical errors. Therefore, we need discover the maximum allowable time step to save the computational cost and keep reasonable accuracy. In Fig. 4.2, we present the energy curves using five different time steps, $\delta t=1e-3$, 5e-4, 2e-4, 1e-4, and 5e-5. When using the tiny time steps 1e-4 and 1e-4, we note both of the energy curves coincide well. But when using 1e-3, 1e-4 and 1e-4, the energy curves derivate viewable away from others. Therefore we will use 1e-4 in the following simulation in order to obtain good accuracy and to consume as low computational cost as possible.

We also note when using the IEQ type scheme, even though the original energy (2.1) and the modified energy (3.2) are equivalent in the PDE level, their discrete cases are not identical indeed. Thus, we also compare the evolutions of the original discrete energy (2.1) and the modified discrete energy (3.23) in Fig. 4.2, where these two curves coincide very well and show monotonic decay to the equilibrium state.

In Fig. 4.3, we show the profiles for the phase field variable ϕ up to the equilibrium state, where snapshots are taken at t=0, 1e-2, 1.5e-2, 2e-2, 4e-2. We observe the coarsening effect that the small circle is absorbed into the big circle smoothly.

4.3. Anisotropic case with the linear regularization

4.3.1. Evolution of a 2D circle

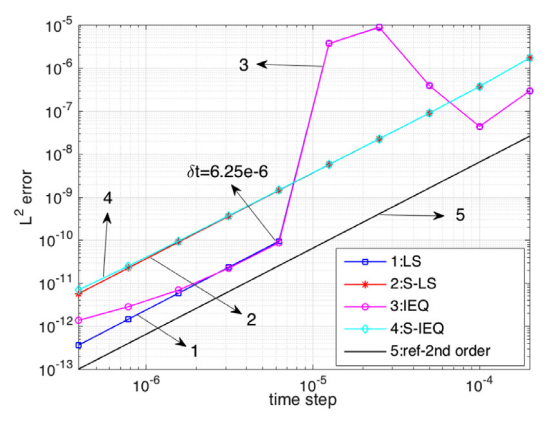
In this example, by using the S-IEQ scheme (3.9)–(3.11) with $S_1 = S_2 = 4$, we compute the simulation for the evolution of a 2D circle for the linear regularization model (3.3)–(3.5). The initial condition is set as

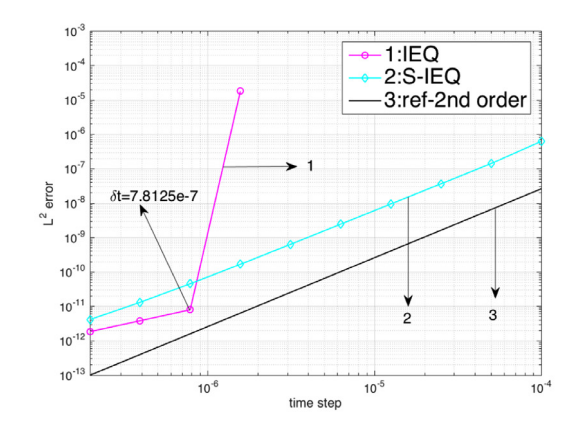
$$\phi_0(x, y) = \tanh\left(\frac{\sqrt{(x-\pi)^2 + (y-\pi)^2} - 0.5\pi}{1.2\epsilon}\right). \tag{4.4}$$

We set $M(\phi) = 1$, $\alpha = 0.3$, $\beta = 6e-4$ and other order parameters are still from (4.1).

In Fig. 4.4, the 2D profile of $\gamma(\mathbf{n}^0)$ and 1D cross-section of $\gamma(\mathbf{n}^0)|_{(\cdot,y=\pi)}$ are presented, and we can observe the high oscillation profile almost everywhere. In Fig. 4.5, we show the dynamics how a circular shape interface with full orientations evolves to an anisotropic pyramid with missing orientations at four corners. Snapshots of the phase field variable ϕ are taken at t=1e-3, 3e-3, 3e-3, and 1e-2. In Fig. 4.6, we show the evolutions of the two free energies, the original energy (2.1) and modified energy (3.23), up to the steady state.

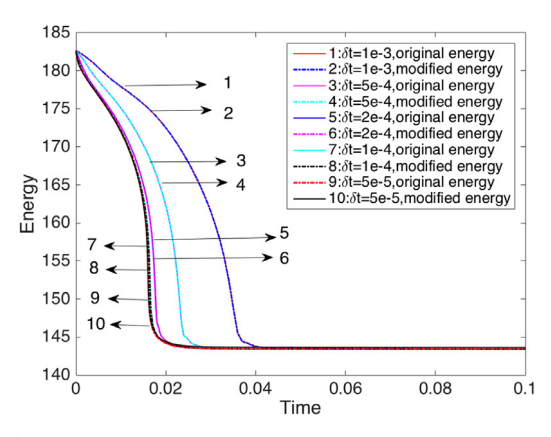
As mentioned in Section 1, the spatial oscillations caused by $\gamma(\mathbf{n})$ can induce severe instability on the time step, therefore the formally energy stable IEQ method still blows up even when using very small time steps. This phenomenon is demonstrated

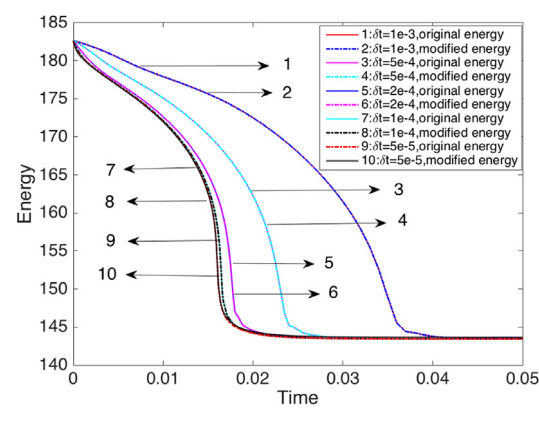




- (a) The L^2 errors for linear regularization model.
- (b) The L^2 errors for Willmore regularization model.

Fig. 4.1. The L^2 numerical errors for the phase variables ϕ at $t=1\mathrm{e}-3$, that are computed using the schemes LS, S-LS, IEQ, and S-IEQ with various time steps and the initial condition (4.2).





- (a) Evolutions of the original energy and the modified energy for $\alpha = 0$ with different δt .
- (b) A close-up view.

Fig. 4.2. Comparisons of the evolutions of the original energy (2.1) and modified energy (3.23) for the isotropic case ($\alpha=0$) with different time steps ($\delta t=1e-3$, 5e-4, 2e-4, 1e-4, 1e-4











Fig. 4.3. Evolution of the interface with the isotropic case ($\alpha = 0$) of two circles. Snapshots of the numerical approximation are taken at t = 0, 1e-2, 1.5e-2, 2e-2, and 4e-2.

in Fig. 4.7, where we use the IEQ scheme ((3.9)–(3.11) with $S_1 = S_2 = 0$) and tiny time steps ($\delta t = 1\text{e}-7$ and 1e-8) to compute the evolutions of the original free energy functional (2.1) and the modified free energy functional (3.23). We observe that, besides the appearance of the strong oscillations, large deviations between the original energy and modified energy emerge as well. Moreover, any computed results with the time step $\delta t > 1\text{e}-7$ are not shown here since they all blow up.

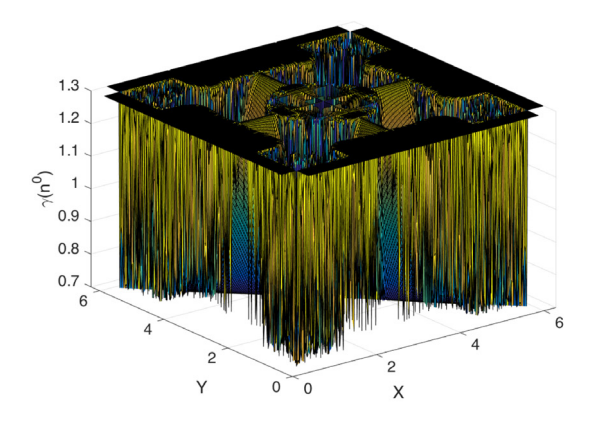
We further show how the spatial oscillations can be eliminated by the combination of stabilizers S_1 and S_2 . In Fig. 4.8, the evolutions of the original energy (2.1) for five combinations of stabilizers are shown: (1) $S_1 = S_2 = 0$; (2) $S_1 = 4$, $S_2 = 0$; (3) $S_1 = 0$, $S_2 = 4$; (4) $S_1 = S_2 = 2$; and (5) $S_1 = S_2 = 4$. For cases (1) and (2), the energies increase with time and present some

non-physical oscillations; for cases (3) and (4), the energy initially decays but further increase and present oscillations; only for case (5), all oscillations vanish and energy decays monotonically, that means the case (5), which is adopted for simulations, is an effective combination of stabilizers to suppress high-frequency oscillations efficiently.

4.3.2. Evolution of two circles in 2D

In this example, we set the initial condition to be two 2D circles with different radii, that reads as

$$\phi_0(x,y) = \sum_{i=1}^{2} \tanh\left(\frac{\sqrt{(x-x_i)^2 + (y-y_i)^2} - r_i}{1.2\epsilon}\right) - 1,$$
 (4.5)



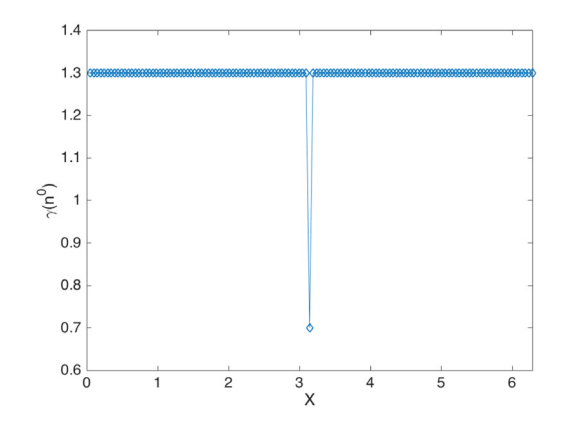
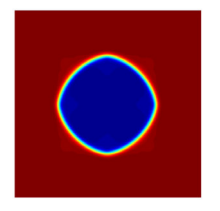


Fig. 4.4. The profile of $\gamma(\mathbf{n}^0)$ with $\alpha=0.3$ by using the initial condition (4.4). The left subfigure is the 2D surface plots of $\gamma(\mathbf{n}^0)$, and the right subfigure is the 1D cross-section of $\gamma(\mathbf{n}^0)|_{(\cdot,y=\pi)}$.



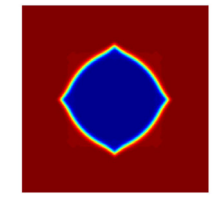
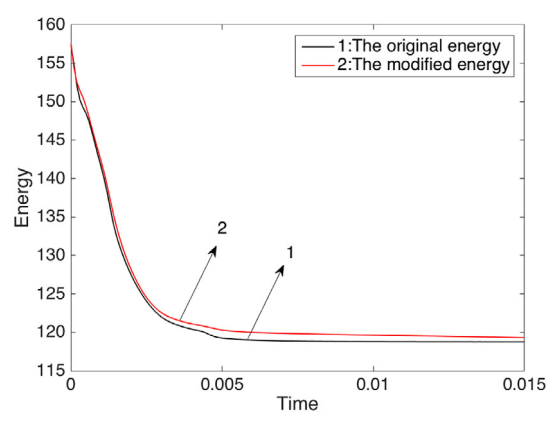
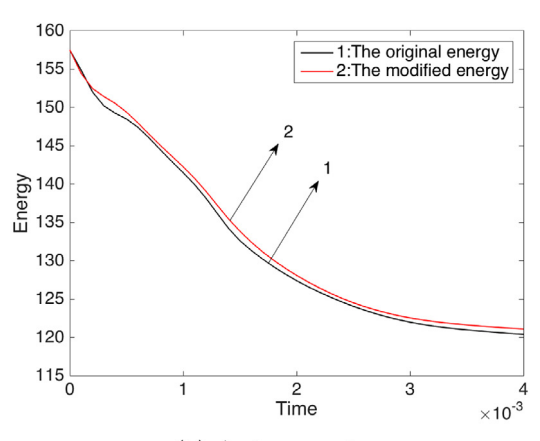






Fig. 4.5. The 2D dynamical evolution of the phase variable ϕ for the anisotropic linear regularization model by using the initial condition (4.4), $\delta t = 1\text{e}-4$, $\alpha = 0.3$, and $\beta = 6\text{e}-4$. Snapshots of the numerical approximation are taken at t = 1e-3, 3e-3, 5e-3, and 1e-2.





(a) Evolutions of the original energy and the modified energy for $\alpha=0.3$.

(b) A close-up view.

Fig. 4.6. Time evolutions of the two free energy functionals, the original energy (2.1) and the modified energy (3.23), for the anisotropic model with linear regularization with $\alpha = 0.3$, $\beta = 6e-4$, $S_1 = S_2 = 4$, and initial condition (4.4). The left subfigure is the energy profile until the equilibrium, and the right subfigure is a close-up view showing where the energy decreases fast.

where $(x_1, y_1, r_1) = (0.8\pi, 1.02\pi, 0.5\pi)$ and $(x_2, y_2, r_2) = (1.67\pi, 0.98\pi, 0.2\pi)$. We vary the parameter α and fix all other parameters from the previous Section 4.3.1. We still keep $S_1 = S_2 = 4$, and the time step is $\delta t = 1e-4$.

In Fig. 4.9(a), we set $\alpha=0.1$, and present snapshots of the profiles of the phase field variable ϕ when t=2e-3, 5e-3, 3.4e-2, 5e-2, and 1.5e-1. We observe that the two circles first evolve to anisotropic shapes with missing orientations at the four corners, then the anisotropic system coarsens and the small shape is absorbed into the big one. In Fig. 4.9(b) and (c), we increase α to 0.2, 0.3, and observe that the facets become more flat and the corners become sharper. In Fig. 4.10, we present the evolutions of the original energy (2.1) and the modified energy (3.23) up to the steady states for these three cases where we can see that the coarsening process is faster for smaller α .

4.3.3. Spinodal decomposition in 2D

In this example, we simulate the phase separation dynamics and the effect of anisotropic terms that is called spinodal decomposition by using the S-IEQ scheme (3.9)–(3.11). The initial condition is taken as the randomly perturbed function as follows,

$$\phi_0(x, y) = \bar{\phi}_0 + 0.001 \text{rand}(x, y),$$
(4.6)

where $\bar{\phi}_0 = 0.5$ and rand(x, y) is the random number which follows the standard uniform distribution on the open interval (0, 1). The order parameters here are the same as Section 4.3.1 and the time step is $\delta t = 1e-4$.

In Fig. 4.11, we show the profiles of the phase field variable ϕ up to the steady state where we can observe the combined effects of anisotropy and coarsening when time evolves. Snapshots of the numerical approximation ϕ are taken at t=1e-2, 1e-1,

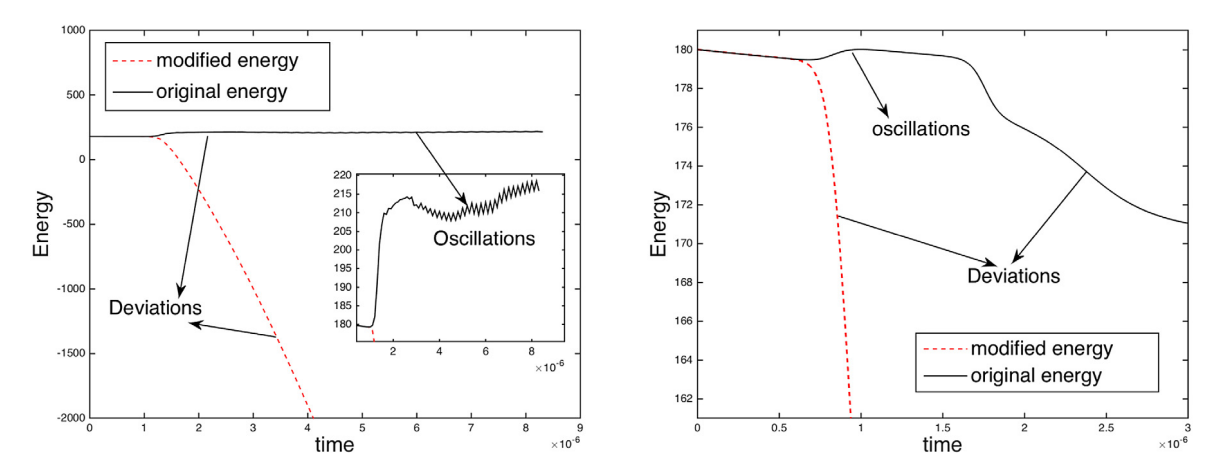


Fig. 4.7. Time evolutions of the two free energy functionals, the modified energy (3.23) and the original energy (2.1), that are computed by the IEQ scheme with $S_1 = S_2 = 0$, $\delta t = 1e-7$ (left) and $\delta t = 1e-8$ (right), for the anisotropic model with linear regularization.

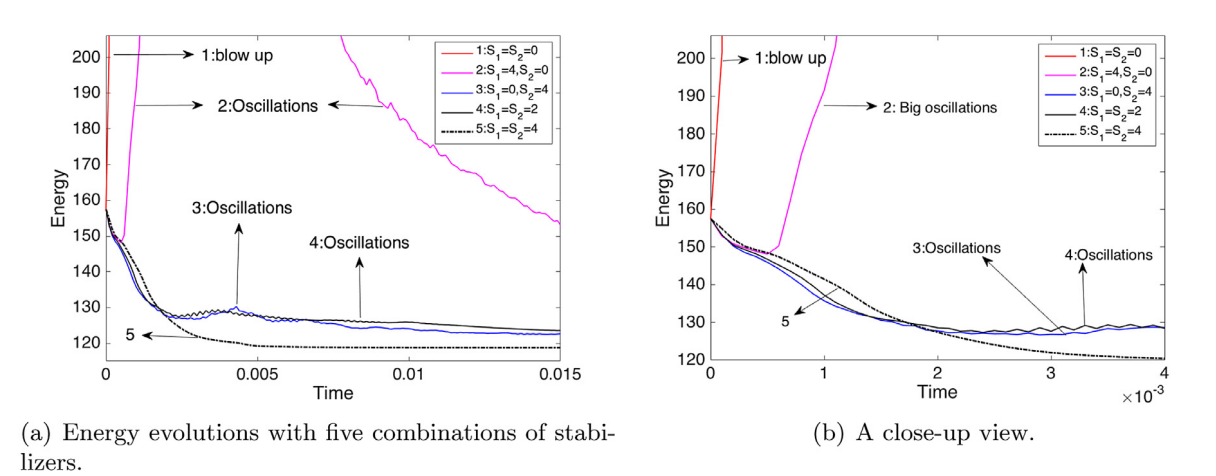


Fig. 4.8. Time evolutions of the original free energy functional (2.1) of five combinations of linear stabilizers, for the anisotropic model with the linear regularization. The left subfigure (a) is the energy profile for $t \in [0, 1.5e-2]$, and the right subfigure (b) is a close-up view for $t \in [0, 4e-3]$.

3e-1, 5e-1, and 1. The final equilibrium solution is obtained after t=7.79e-1, where the equilibrium shape becomes a pyramid due to the strong anisotropy. In Fig. 4.12, we plot the evolutions of the original energy (2.1) and the modified energy (3.23), which show the decays with time that confirms that our algorithms are unconditionally stable.

4.3.4. Evolution of a 3D sphere

In this example, we investigate the 3D simulations of a sphere by using the following initial condition

$$\phi_0(x, y, z) = \tanh\left(\frac{\sqrt{(x-\pi)^2 + (y-\pi)^2 + (z-\pi)^2} - 0.5\pi}{\epsilon}\right). \tag{4.7}$$

We use 128^3 grid points to discretize the computational domain and the time step is $\delta t = 1e-4$. We vary the magnitude of α and β , and other order parameters are still from Section 4.3.1.

First, we set $\alpha=0.1$ and $\beta=6\mathrm{e}-4$, the evolution of the spherical shape towards its equilibrium is shown in Fig. 4.13(a), where we observe that the 3D sphere evolves to an anisotropic octahedron with missing orientations. We further fix $\beta=6\mathrm{e}-4$ and increase $\alpha=0.3$, the octahedrons become more flat and the edges become sharper, shown in Fig. 4.13(b). At last, we fix $\alpha=0.3$, and increase $\beta=6\mathrm{e}-3$, the edges become more smooth, shown in Fig. 4.13(c).

4.4. Willmore regularization model

In this subsection, we consider the anisotropic system with the Willmore regularization.

4.4.1. Evolution of a 2D circle

In this example, by using the S-IEQ scheme (3.36)–(3.38), we compute the simulation for the evolution of a 2D circle, where the initial condition is set as

$$\phi_0(x, y) = \tanh(\frac{\sqrt{(x-\pi)^2 + (y-\pi)^2} - 0.5\pi}{1.2\epsilon}),\tag{4.8}$$

and the order parameters are set as

$$\epsilon = 6.28e-2, \ \beta = 6e-4, \ B = 1e4,
S_1 = S_2 = 4, \ S_3 = 4e-3, \ \delta t = 5e-5.$$
(4.9)

We investigate the impacts of the strength of the anisotropy parameter α and the Willmore regularization parameter β on the equilibrium fourfold shapes. We choose three different values of $\alpha=0.1,\,0.2,\,0.3,\,$ and fix $\beta=6e-4,\,$ the equilibrium shapes are compared in Fig. 4.14. It can be observed that the increase of α leads to a pyramid with shaper corners and smoother facets because of the strong anisotropy. The evolutions of the original energy (2.1) and the modified energy (3.41) are shown in Fig. 4.15, where we observe that the energy decreases faster with larger α .

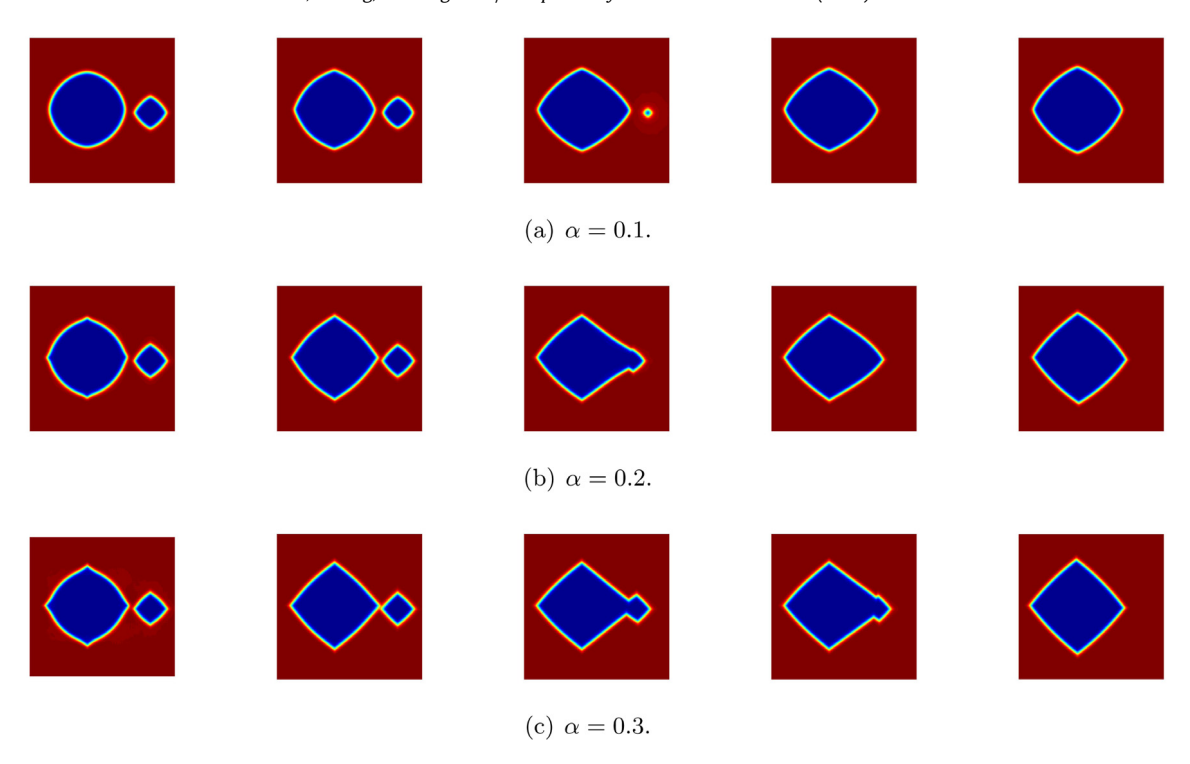


Fig. 4.9. The 2D dynamical evolutions of the phase variable ϕ with $\alpha=0.1,0.2$, and $\alpha=0.3$. The snapshots of the numerical approximation are taken at t=2e-3,5e-3,3.4e-3,5e-2, and 1.5e-1.

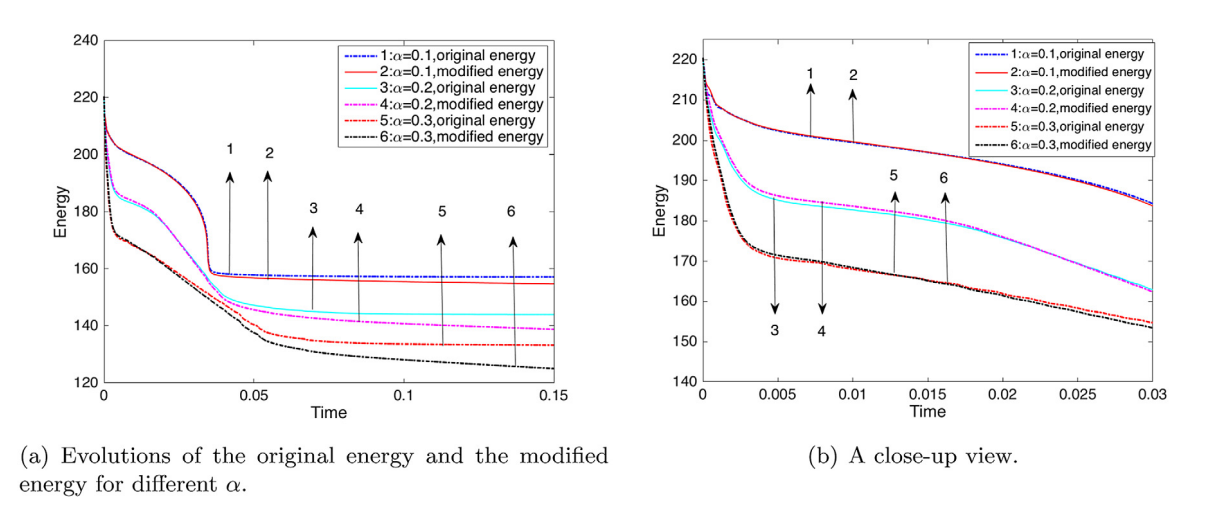


Fig. 4.10. Time evolutions of the two free energy functionals, the original energy (2.1) and the modified energy (3.23) for the linear regularization with $\alpha = 0.1, 0.2, 0.3, \beta = 6e-4$, and initial condition (4.5). The left subfigure (a) is the energy profile for $t \in [0, 1.5e-1]$, and the right subfigure (b) is a close-up view for $t \in [0, 3e-2]$.

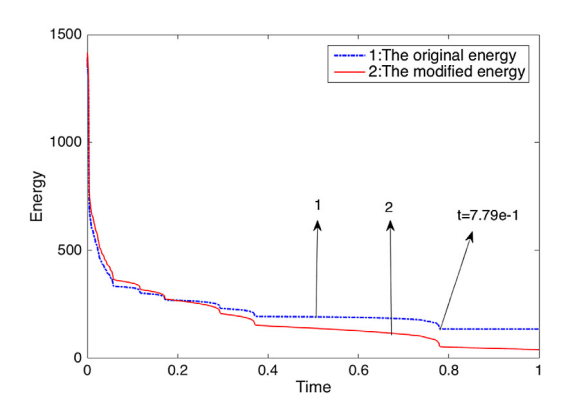


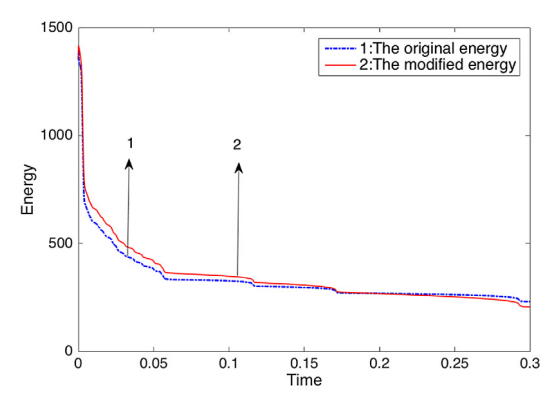
Fig. 4.11. The 2D dynamical evolution of the phase variable ϕ of the spinodal decomposition example for the linear regularization model, by using the initial condition (4.6), $\delta t = 1e-4$, $\alpha = 0.3$, and $\beta = 6e-4$. Snapshots are taken at t = 1e-2, 1e-1, 1e-1

In Fig. 4.16, we show the effects of the Willmore regularization parameter β on the equilibrium shapes, in which, we choose $\beta=3e-4$, 6e-4, 1.2e-3, 2.4e-3, and fix $\alpha=0.4$. There are no visible differences with respect to the facets, but the corners become sharper in the equilibrium morphologies, as β decreases. The

corresponding original energy evolutions are plotted in Fig. 4.17, where one can observe that energy decreases faster with smaller β .

A closer look at Fig. 4.16 also indicates that the numerical solution with the Willmore regularization converges to the asymptotic solution as β approaches to zero. At the same time, the edges





(a) Time evolutions of the original energy and the modified energy of the spinodal decomposition example.

(b) A close-up view.

Fig. 4.12. Time evolutions of the two free energy functionals, the original energy (2.1) and the modified energy (3.23), of the spinodal decomposition example for the linear regularization model by using the initial condition (4.6). The left subfigure (a) is the energy profile for $t \in [0, 1]$, and the right subfigure (b) is a close-up view for $t \in [0, 3e-1]$.

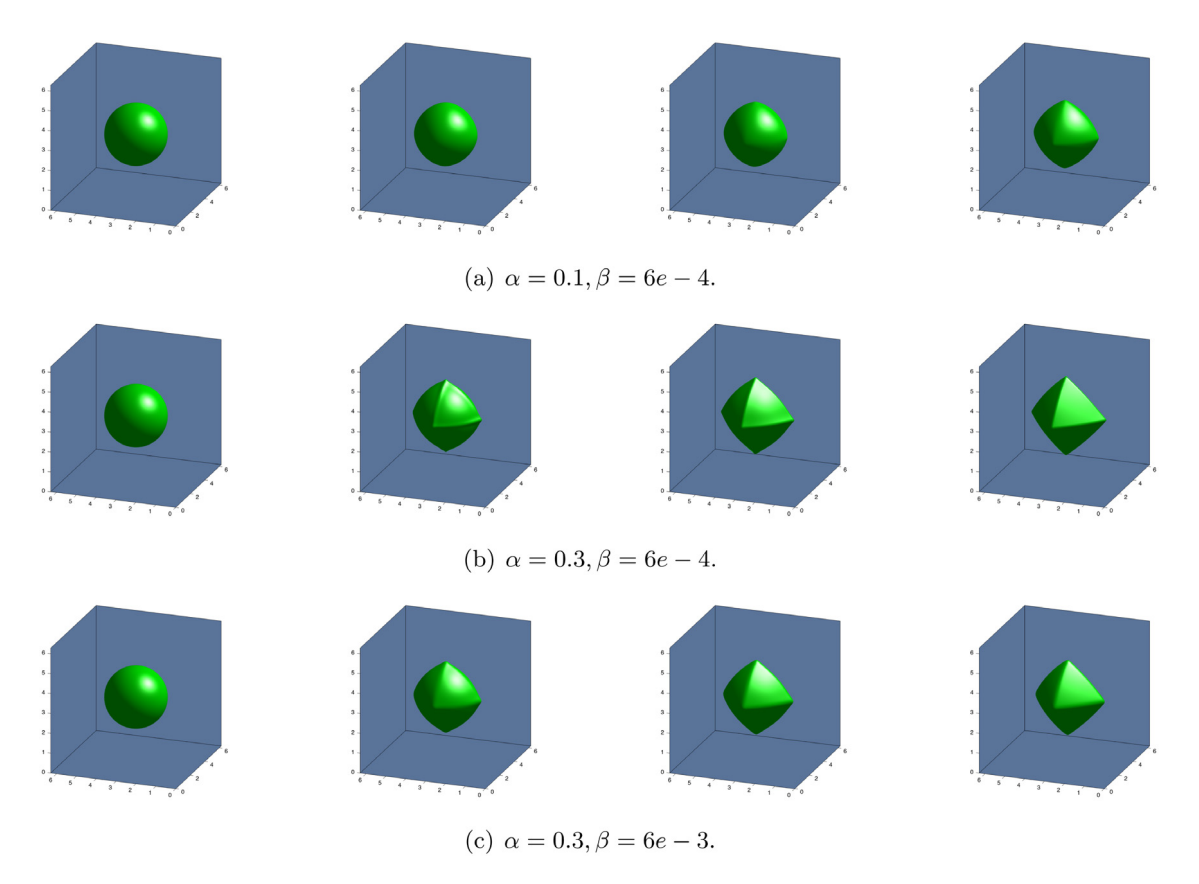


Fig. 4.13. The dynamical evolution of a 3D sphere for the anisotropic linear regularization model, by using the initial condition (4.7), and $\delta t = 1e-4$. (a) $\alpha = 0.1$, $\beta = 6e-4$; (b) $\alpha = 0.3$, $\beta = 6e-4$; and (c) $\alpha = 0.3$, $\beta = 6e-3$. Snapshots of the isosurfaces of the phase field variable $\{\phi = 0\}$ are taken at t = 0, 2e-2, 4e-2, and 1e-1.

and corners match the asymptotic result more closely than in the linear regularization, which can be seen in Fig. 4.18. All these observations are in good agreements with the numerical results presented in [2,29,31].

4.4.2. Roughing process of a smooth curve

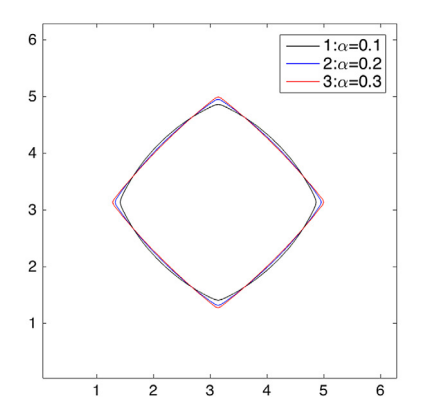
In this example, we use the Willmore regularization model to examine evolution of a smooth interface to facets. The initial condition reads as

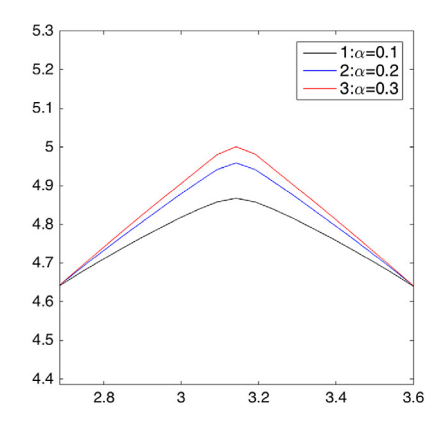
$$\phi_0(x, y) = \tanh(-(y - 1.4\pi - 0.2r(x))/\epsilon) + \tanh((y - 0.6\pi - 0.2r(x))/\epsilon) - 1,$$
(4.10)

where $r(x) = 1.8\pi \cos(2x) + 1.5\pi \cos(6x) + 0.4\pi \cos(6x) + 0.1\pi \cos(14x)$, and the order parameters are set as

$$\epsilon = 6.28e-2$$
, $\alpha = 0.3$, $\beta = 4e-4$, $\delta t = 1e-6$, $B = 1e4$, $S_1 = S_2 = 4$, $S_3 = 4e-3$.

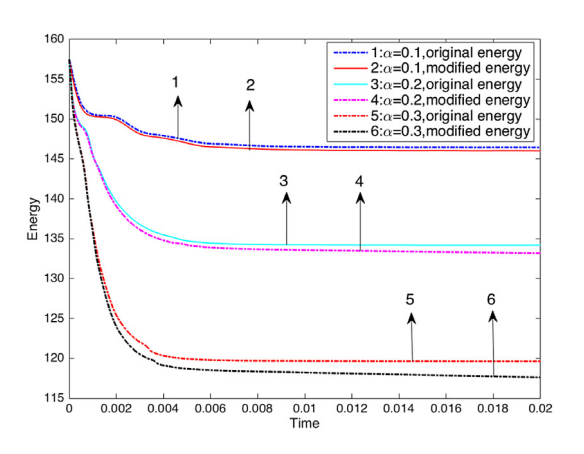
The profiles of the phase field variable ϕ up to the steady state are shown in Fig. 4.19, where the initially smooth interface quickly forms many small facets along the low-energy orientations. Sooner after that, the small facets evolve into larger ones. Finally, the equilibrium shape is dominated by the largest initial mode, which is $1.8\pi\cos(2x)$. These simulations are consistent with the computed results in [2,29,31].

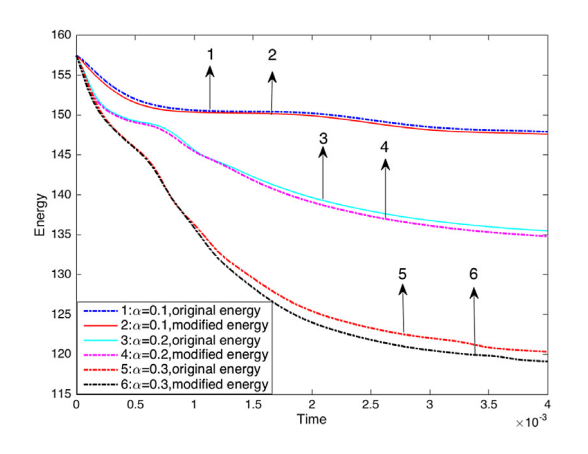




- (a) The contours of $\{\phi=0\}$ of the equilibrium solutions with different α .
- (b) A close-up view.

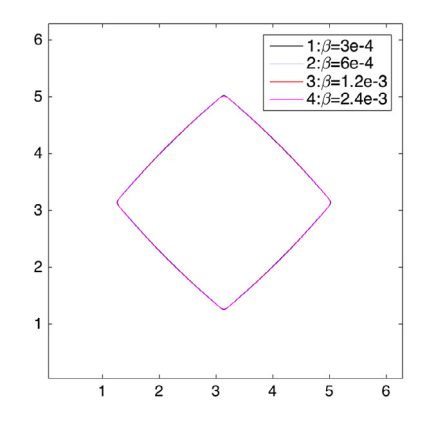
Fig. 4.14. The contours of $\{\phi = 0\}$ of the equilibrium solutions for the anisotropic model with the Willmore regularization by using the initial condition (4.8), $\beta = 6e-4$ and three different values $\alpha = 0.1$, 0.2, and 0.3. The right subfigure (b) is the close-up view, for the top corner of the left subfigure (a).

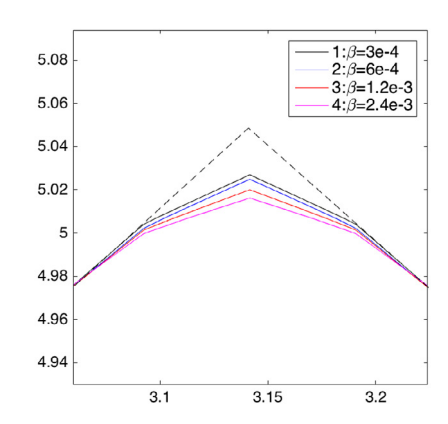




- (a) Time evolutions of the original energy and the modified energy for different α .
- (b) A close-up view.

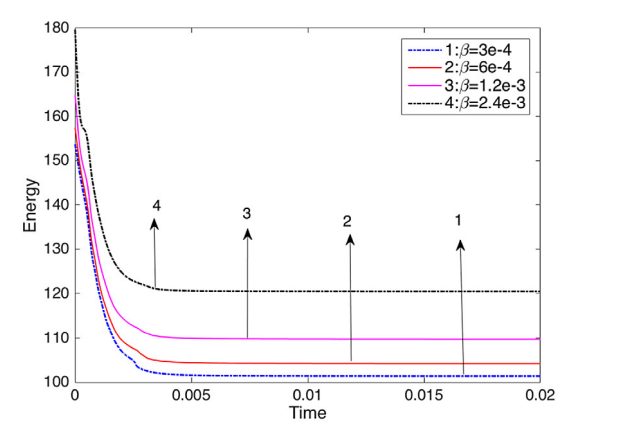
Fig. 4.15. Time evolutions of the two free energy functionals, the original energy (2.1) and the modified energy (3.41), for the 2D circle example of the anisotropic model with the Willmore regularization, by using the initial condition (4.8), $\beta = 6e-4$ and three different values $\alpha = 0.1$, 0.2, 0.3. The left subfigure (a) is the energy profile for $t \in [0, 2e-2]$, and the right subfigure (b) is a close-up view for $t \in [0, 4e-3]$.

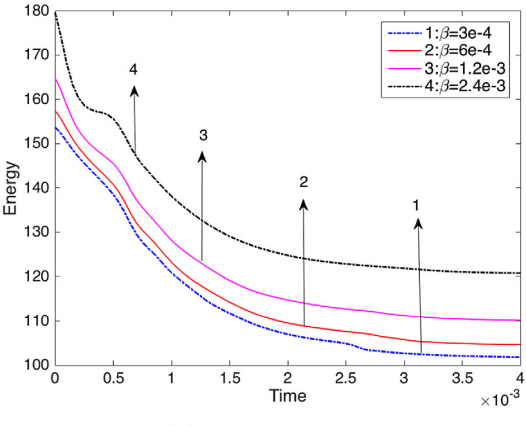




- (a) The contours of $\{\phi=0\}$ of the equilibrium solutions with different $\beta.$
- (b) A close-up view.

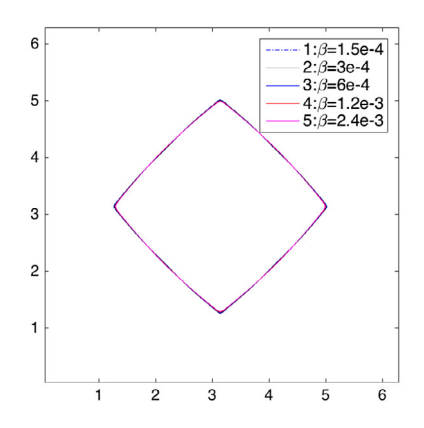
Fig. 4.16. The contours of $\{\phi = 0\}$ of the equilibrium solutions for the anisotropic model with the Willmore regularization by using the initial condition (4.8), $\alpha = 0.4$ and four different values $\beta = 3e-4$, 6e-4, 1.2e-3, and 2.4e-3. The right subfigure (b) is the close-up view, for the top corner of the left subfigure (a).

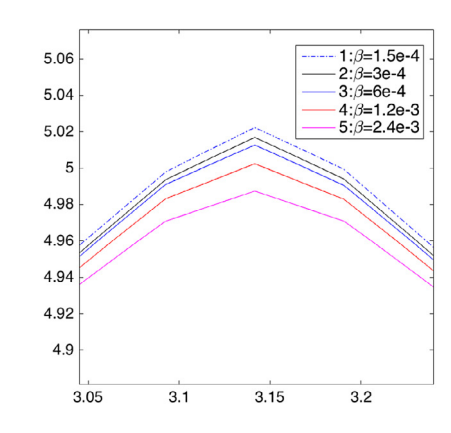




- (a) Time evolutions of the original energy for different β .
- (b) A close-up view.

Fig. 4.17. Time evolutions of the original free energy functional (2.1) for the 2D circle example of the anisotropic model with the Willmore regularization, by using the initial condition (4.8), $\alpha = 0.4$ and four different values $\beta = 3e-4$, 6e-4, 1.2e-3, and 2.4e-3. The left subfigure (a) is the energy profile for $t \in [0, 2e-2]$, and the right subfigure (b) is a close-up view for $t \in [0, 4e-3]$.





- (a) The contours of $\{\phi=0\}$ of the equilibrium solutions with different β .
- (b) A close-up view.

Fig. 4.18. The contours of $\{\phi=0\}$ of the equilibrium solutions for the anisotropic model with the linear regularization by using the initial condition (4.8), $\alpha=0.4$ and five different values $\beta=1.5e-4$, 3e-4, 6e-4, 1.2e-3, and 2.4e-3. The right subfigure (b) is the close-up view, for the top corner of the left subfigure (a).

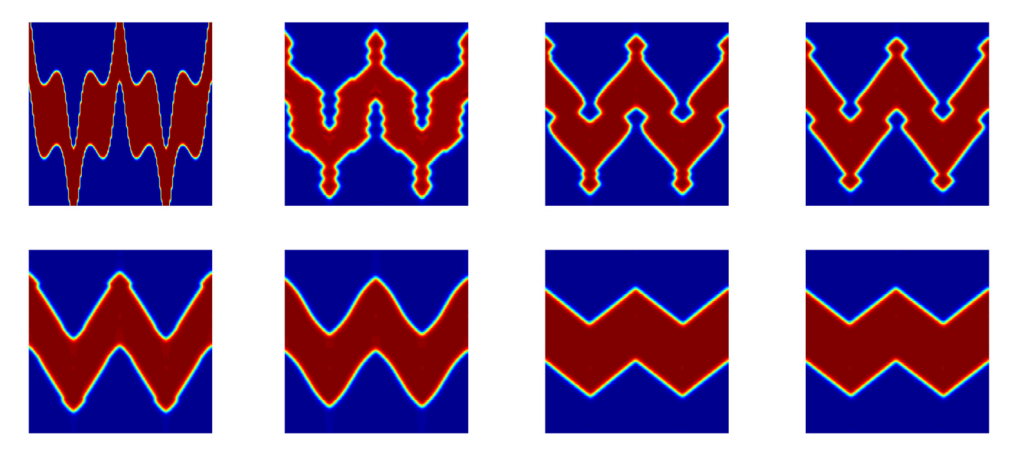


Fig. 4.19. The 2D dynamical evolution of the phase variable ϕ of the roughing curve example for the anisotropic Willmore regularization model, by using the initial condition (4.10). Snapshots are taken at t=0, 5e-5, 8e-5, 1e-4, 1.5e-4, 2e-4, 5e-4, and 1e-3.

5. Concluding remarks

In this paper, we develop two second-order, stabilized-IEQ schemes to solve the anisotropic Cahn-Hilliard system by combining the IEQ approach with the stabilization technique. Some

linear stabilizers are added which are shown to be very crucial to suppress the non-physical oscillations caused by the strong anisotropic coefficient. The proposed schemes (i) are accurate (second-order in time); (ii) are stable (the unconditional energy dissipation law holds); and (iii) are easy to implement (only need

to solve linear equations at each time step). Furthermore, the induced linear system is well-posed, thus one can apply any Krylov subspace method with mass lumping as pre-conditioner for solving such system efficiently. We perform a number of numerical simulations in 2D and 3D to demonstrate the efficiency, accuracy and energy stability for the schemes. Moreover, the proposed method can be extended to develop linear schemes for a large class of gradient flow problems with complex nonlinearities in the free energy density. The related error analysis work, including the semi-discrete scheme and fully-discrete schemes in the context of finite element method or spectral method, is expected to be implemented in the future by following the same line of procedure as [35–40].

Acknowledgments

Z. Xu is partially supported by China Scholarship Council (No. 201706040140). X. Yang is partially supported by National Science Foundation (NSF) DMS-1720212 and 1818783. H. Zhang is partially supported by NSFC-11471046 and NSFC-11571045. Z. Xie is partially supported by NSFC-11771138, NSFC-11171104, and NSFC-91430107.

References

- [1] S. Torabi, J. Lowengrub, A. Voigt, S. Wise, Proc. R. Soc. Lond. Ser. A Math. Phys. Eng. Sci. 465(2105) (2009) 1337–1359.
- [2] S. Wise, J. Kim, J. Lowengrub, J. Comput. Phys. 226(1) (2007) 414-446.
- [3] J.E. Taylor, J.W. Cahn, Physica D 112(3-4)) (1998) 381-411.
- [4] Q. Du, C. Liu, X. Wang, J. Comput. Phys. 198 (2004) 450-468.
- [5] C. Miehe, M. Hofacker, F. Welschinger, Comput. Methods Appl. Mech. Engrg. 199 (2010) 2765–2778.
- [6] J.S. Lowengrub, A. Ratz, A. Voigt, Phys. Rev. E 79 (3) (2009).
- [7] J. Shen, X. Yang, Discrete Contin. Dyn. Syst. Ser. B 28 (2010) 1669-1691.
- [8] X. Feng, A. Prol, Numer. Math. 94 (2003) 33-65.
- [9] D. Han, X. Wang, J. Comput. Phys. 290 (2015) 139-156.

- [10] D.J. Eyre, Computational and Mathematical Models of Microstructural Evolution (San Francisco, CA, 1998), in: Mater. Res. Soc. Sympos. Proc., vol. 529, MRS, Warrendale, PA, 1998, pp. 39–46.
- 11] J. Zhao, X. Yang, J. Shen, Q. Wang, J. Comput. Phys. 305 (2016) 539-556.
- [12] J. Zhao, X. Yang, J. Li, Q. Wang, SIAM. J. Sci. Comput. 38 (2016) A3264-A3290.
- [13] J. Shen, C. Wang, S. Wang, X. Wang, SIAM J. Numer. Anal. 50 (2012) 105–125.
- [14] D. Han, A. Brylev, X. Yang, Z. Tan, J. Sci. Comput. 70 (2017) 965–989.
- [15] Q. Huang, X. Yang, X. He, Discrete Contin. Dyn. Syst. Ser. B 23 (2018) 2177–2192.
- [16] Y. Gao, X. He, L. Mei, X. Yang, SIAM. J. Sci. Comput. 40 (2018) B110?B137.
- [17] X. Yang, D. Han, J. Comput. Phys. 330 (2017) 1116-1134.
- [18] X. Yang, L. Ju, Comput. Methods Appl. Mech. Engrg. 315 (2017) 691-712.
- [19] X. Yang, J. Comput. Phys. 327 (2016) 294-316.
- [20] X. Yang, J. Zhao, X. He, J. Comput. Appl. Math. 343 (2018) 80–97.
- [21] X. Yang, J. Zhao, Q. Wang, J. Comput. Phys. 333 (2017) 104-127.
- [22] J. Zhao, Q. Wang, X. Yang, Internat. J. Numer. Methods Engrg. 110 (2017) 279–300.
- [23] X. Yang, J. Zhao, Q. Wang, J. Shen, M3AS: Mathematical Models and Methods in Applied Sciences 27 (2017) 1993.
- [24] J. Zhao, X. Yang, Y. Gong, Q. Wang, Comput. Methods Appl. Mech. Engrg. 318 (2017) 803–825.
- [25] L. Chen, J. Zhao, X. Yang, Appl. Numer. Math. 128 (2018) 139-156.
- [26] J. Shen, J. Xu, J. Yang, J. Comput. Phys. 353 (2018) 407-416.
- [27] J.J. Eggleston, G.B. McFadden, P.W. Voorhees, Physica D 150(1-2)) (2001) 91–103.
- [28] J.W. Barrett, H. Garcke, R. Nurnberg, ZAMM. Z. Angew. Math. Mech 93 (2013) 719–732.
- [29] F. Chen, J. Shen, Commun. Comput. Phys. 05 (2013) 1189-1208.
- [30] Y. Chen, J. Lowengrub, J. Shen, C. Wang, Steven Wise, J. Comput. Phys. 365 (2018) 56–73.
- [31] J. Shen, J. Xu, Commun. Comput. Phys. 24 (3) (2018) 635–654.
- [32] X. Yang, L. Ju, Comput. Methods Appl. Mech. Engrg. 318 (2017) 1005-1029.
- [33] X. Yang, J. Sci. Comput 74 (2017) 1533-1553.
- [34] Q. Cheng, X. Yang, J. Shen, J. Comput. Phys. 341 (2017) 44-60.
- [35] R. Zhang, D. Zeng, S. Zhong, Y. Yu, Appl. Math. Comput. 310 (2017) 57–74.
- [36] Y. Bai, Y. Wu, X. Xie, Sci. China Math. 59 (2016) 1835–1850.
- [37] H. Geng, T. Yin, L. Xu, J. Comput. Appl. Math. 313 (2017) 1–17.
- [38] C.Y Wu, T.-Zh. Huang, Ukr. Math. Bull. 68 (2017) 1949–1964.
- [39] M. Li, P. Guyenne, F. Li, L. Xu, J. Sci. Comput. 71 (2017) 994–1034.
- [40] C. Chen, X. He, J. Huang, Appl. Numer. Math. 96 (2015) 165–179.